Chinese Chemical Letters 37 (2026) 111214

Contents lists available at ScienceDirect

Chinese Chemical Letters

journal homepage: www.elsevier.com/locate/cclet

Molecular engineering organometallic sonosensitizer for enhanced sonodynamic therapy *via* promoting ER stress-mediated HIF-1α degradation and cGAS-STING pathway activation

Yubo Tan[a,d,1], Ziying Wang[e,1], Yibo An[a,f,1], Man Li[d], Dazhuang Xu[b], Renyuan Liu[a], Xinyu Tan[d], Yaohui He[c,*], Zhixiang Lu[a,f,*], Gang Liu[b,*]

[a] State Key Laboratory of Vaccines for Infectious Diseases & Fujian Provincial Key Laboratory of Innovative Drug Target Research, School of Pharmaceutical Sciences, Xiamen University, Xiamen 361102, China
[b] State Key Laboratory of Molecular Vaccinology and Molecular Diagnostics & Center for Molecular Imaging and Translational Medicine, School of Public Health, Xiamen University, Xiamen 361102, China
[c] Institute for Future Sciences, University of South China, Changsha 410008, China
[d] School of Life Sciences, Xiamen University, Xiamen 361102, China
[e] Key Laboratory for Regenerative Medicine of the Ministry of Education of China, School of Biomedical Sciences, Faculty of Medicine, The Chinese University of Hong Kong, Hong Kong 999077, China
[f] Sichuan Research Institute of Xiamen University, Chengdu 610000, China

ARTICLE INFO

Article history:
Received 28 November 2024
Revised 14 April 2025
Accepted 15 April 2025
Available online 17 April 2025

Keywords:
Sonodynamic therapy
Endoplasmic reticulum-stress
cGAS-STING
HIF-1α
Anti-tumor immunity

ABSTRACT

Given the immense potential of sonodynamic therapy (SDT) in cancer treatment, designing effective sonosensitizers (SNSs) and elucidating their mechanisms are crucial for advancing the field and enhancing anti-tumor responses. However, there are still several limitations that hinder the application of SDT, such as the activation of the hypoxia-inducible factor-1 (HIF-1) pathway. Herein, we designed an endoplasmic reticulum (ER)-targeted iridium(III) SNS, C_6IrAC, which exhibits specific toxicity towards tumor cells and excellent performance as a SNS. C_6IrAC specifically targets the ER, causing ER stress, and under ultrasound (US) stimulation, the increased stress intensity enhances therapeutic efficacy. C_6IrAC induces the degradation of HIF-1α and suppresses the HIF-1 pathway, thereby enhancing SDT. Furthermore, C_6IrAC-induced ER stress leads to mitochondrial calcium overload, which subsequently results in the release of a large amount of mitochondrial DNA (mtDNA) into the cytoplasm, thereby activating the cyclic GMP-AMP synthase (cGAS)-stimulator of interferon genes (STING) pathway. Significant anti-tumor effects have been consistently observed both *in vitro* and *in vivo*. C_6IrAC can effectively activate both the innate and adaptive immune systems, highlighting its substantial therapeutic potential. Taken together, this study provides a feasible method to overcome the limitations of SDT, and opens up new avenues for the design of SNSs.

© 2025 Published by Elsevier B.V. on behalf of Chinese Chemical Society and Institute of Materia Medica, Chinese Academy of Medical Sciences.

Sonodynamic therapy (SDT), which leverages the synergistic effects of ultrasound (US) and sonosensitizers (SNSs), effectively overcomes the limitations associated with traditional photodynamic therapy (PDT) [1,2]. US accurately targets the tumor region, activating the SNS to kill tumor cells [1,3]. Due to its non-invasiveness and better therapeutic effect on deep tumors, SDT may become a promising potential cancer treatment method. Many studies have shown that SDT not only directly kills cancer cells, but also regulates the tumor microenvironment (TME) to enhance efficacy [4–6]. SDT can efficiently induce immunogenic cell death (ICD) to promote inflammatory cell infiltration [7–9]. Tumor cells undergoing ICD can release a variety of damage-associated molecular patterns (DAMPs), such as high-mobility group box 1 (HMGB1) and calreticulin (CRT) [10,11]. These DAMPs effectively promote dendritic cells (DCs) maturation, and subsequently facilitating the infiltration of T cells into the tumor and activating anti-tumor immunity [12]. In addition, SDT can also inhibit tumor angiogenesis to a certain extent [13]. However, SDT generally consumes oxygen during the induction of cytotoxicity, exacerbating hypoxia within solid tumors, which in turn further activates the hypoxia-inducible factor-1 (HIF-1) pathway in tumor cells [14]. It is known

* Corresponding authors.
E-mail addresses: 2024001050@usc.edu.cn (Y. He), zhixiangl@xmu.edu.cn (Z. Lu), gangliu.cmitm@xmu.edu.cn (G. Liu).
[1] These authors contributed equally to this work.

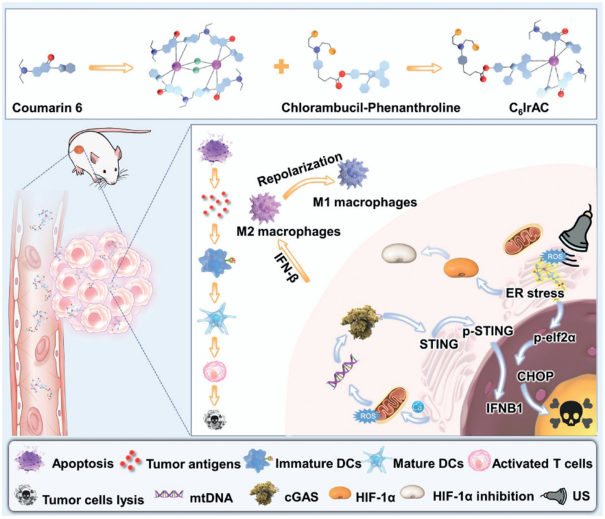
https://doi.org/10.1016/j.cclet.2025.111214
1001-8417/© 2025 Published by Elsevier B.V. on behalf of Chinese Chemical Society and Institute of Materia Medica, Chinese Academy of Medical Sciences.

that the HIF-1 pathway is activated under hypoxic conditions and then maintained stable, endowing tumor cells with a survival advantage, accelerating their migration and invasion, as well as suppressing immunity and promoting evasion [15,16]. These factors make the application of SDT still several limitations. Importantly, the sonodynamic properties of the SNS also play a key role in the treatment process. Thus, inhibiting HIF-1 pathway and developing high-performance SNSs are very important for synergistic SDT [17].

The latest studies have elucidated that endoplasmic reticulum (ER) stress can promote the proteasomal degradation of HIF-1α [18]. It is important to note that the potential for mitigating challenges faced by SDT through endoplasmic reticulum stress-induced HIF-1α degradation has not been fully explored, which would be very meaningful research. In-depth investigation of the interplay between ER stress and the HIF-1 pathway may provide novel insights and strategies for more effective SDT, warranting further research. Moreover, ER stress is closely associated with ICD, triggering the unfolded protein response (UPR) and the effective release of DAMPs [19]. Besides, ER stress has long been implicated in the activation of the cyclic GMP-AMP synthase (cGAS)-stimulator of interferon genes (STING) pathway, but whether ER stress activates the cGAS-STING pathway remains to be definitively explored [20].

The cGAS-STING pathway is a key mediator in triggering the innate immune response [21]. The activation of STING stimulates the release of type I interferons (IFN) [22], recruits T cells for tumor infiltration, promotes the maturation of DCs [23], and polarizes tumor-associated macrophages towards an anti-tumor M1 macrophage phenotype [24]. Recently, the therapeutic strategy employing STING agonists has been demonstrated to be effective in eradicating residual cancer cells and preventing metastatic relapse [25,26]. These exciting advancements substantiate the efficacy of activating the cGAS-STING signaling pathway as a potential oncological treatment modality. However, the performance of monotherapy with STING agonists in clinical trials has not met the anticipated outcomes. It suggests that activation of the STING pathway may require a combination with existing cancer treatment modalities to enhance anti-tumor efficacy [27].

Metal-organic complexes, such as iridium, platinum and rhenium, have shown immense potential as effective SNSs due to their superior reactive oxygen species (ROS) generation efficiency and potent tumoricidal properties [28–30]. Iridium(III) complexes possess a long-lived triplet excited state that facilitates energy transfer with molecular oxygen to produce singlet oxygen ($^1O_2$) [31]. Therefore, iridium(III) complexes have an advantage over other metal elements as SNSs or photosensitizers. Given the potential of ER stress in degrading HIF-1α and its implications for SDT, we have developed an ER-targeting SNS (C_6IrAC) [32]. The chlorambucil structure endows C_6IrAC specific ER targeting capability, thereby inducing ER stress and subsequent apoptosis in tumor cells. Under US treatment, the *in situ* burst of ROS in the ER further aggravates oxidative stress and cell apoptosis. A large number of research evidence confirmed that C_6IrAC significantly amplifies the ICD effect and releases a substantial amount of DAMPs. C_6IrAC-induced ER stress activates the cGAS-STING pathway, releasing abundant type I IFN, thereby activating innate immunity. Concurrently, C_6IrAC promotes the degradation of HIF-1α, effectively inhibiting the HIF-1 pathway, and thus enhanced SDT to suppress the survival, migration and immune evasion of tumor cells. Taken together, the main focus of our current study is illustrated in Scheme 1: (1) A specific SNS targeting the ER, C_6IrAC, was designed based on theoretical calculations. Synthesized C_6IrAC was utilized for fluorescence imaging-guided SDT *in vivo*. (2) C_6IrAC induces ER stress to directly kill cancer cells and triggers ICD, reshaping the tumor immune microenvironment. (3) We propose for the first time that inducing ER stress through an ER-targeting SNS can activate the cGAS-STING pathway and suppress the HIF-1 pathway. The multifunctional ER-targeting iridium(III) SNS provides a compelling alternative strategy for treating cancer by enhancing ER stress and offers a feasible approach to overcoming the limitations of SDT, paving a new avenue for the design of SNSs.



Scheme 1. Schematic representation of the treatment of cancer with the organometallic SNS C_6IrAC, illustrating the mechanism by which C6IrAC induces ER stress and enhances ER stress-mediated innate and adaptive anti-tumor immunity, as well as promotes the degradation of HIF-1α.

The synthesis route of the ER-targeting organometallic SNS C_6IrAC was depicted in Scheme S1 (Supporting information). The successful synthesis of the chromophore C_6IrAC has been corroborated by ^{1}H nuclear magnetic resonance spectroscopy (NMR), ^{13}C NMR and high-resolution mass spectrometry (HRMS) analysis (Figs. S1 and S2a in Supporting information). To further investigate the physicochemical properties of C_6IrAC, theoretical calculations of its energy levels were performed using the density functional theory (DFT) method with the PBE0 (D3BJ)/6–31 (d) basis set as implemented in Gaussian 09 (version E01). The highest occupied molecular orbital (HOMO) of C_6IrAC is localized on the phenanthroline ligand, whereas the lowest unoccupied molecular orbital (LUMO) is delocalized across the iridium atom and the coumarin moiety, suggesting efficient intramolecular charge transfer within the molecular framework (Fig. 1a, Figs. S2b and c in Supporting information). Electrostatic potential (ESP) analysis was conducted to elucidate the distribution of electron density within the C_6IrAC molecule (Fig. 1a). The negative electrostatic potential is predominantly localized on the oxygen atoms of the coumarin moiety, while the positive electrostatic potential exhibits a more dispersed distribution. The HOMO-LUMO and electron density for coumarin and chlorambucil groups were shown in Figs. S2b and c. The energy gaps for C_6IrAC, coumarin, and chlorambucil group were calculated to be 1.294, 3.788, and 5.529 eV, respectively. Notably, the energy gap of C_6IrAC is significantly lower compared to the other two compounds, suggesting that C_6IrAC can be easily excited by stimuli at lower energy levels. The ultraviolet-visible (UV–vis) spectrum of C_6IrAC in phosphate-buffered saline (PBS) exhibits notable absorption within the 400–525 nm wavelength range, with a pronounced absorption peak centered at approximately 480 nm (Fig. 1b). Upon excitation at 480 nm, the fluorescence emission spectrum of C_6IrAC is characterized by a peak around 590 nm (Fig. 1c).

To evaluate the sonodynamic performance of C_6IrAC, 1,7-dichlorodihydrofluorescein diacetate (DCFH-DA) was utilized as a probe to assess the ROS generation capability of C_6IrAC upon US activation. The characteristic peak of DCF at 525 nm exhibited a progressive increase with time throughout US stimulation, which

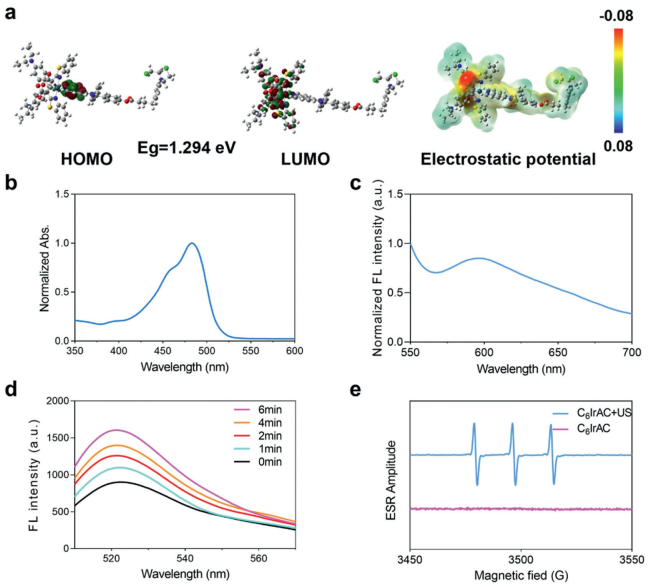


Fig. 1. (a) Theoretical calculations of C_6IrAC, including energy levels and ESP. (b) The normalized UV–vis absorption spectra of C_6IrAC. (c) The normalized emission spectra of C_6IrAC. (d) The time-dependent oxidation of DCFH-DA detecting ROS generation by C_6IrAC under US irradiation. (e) ESR spectrum of C_6IrAC with or without US (TEMP as the detection probe).

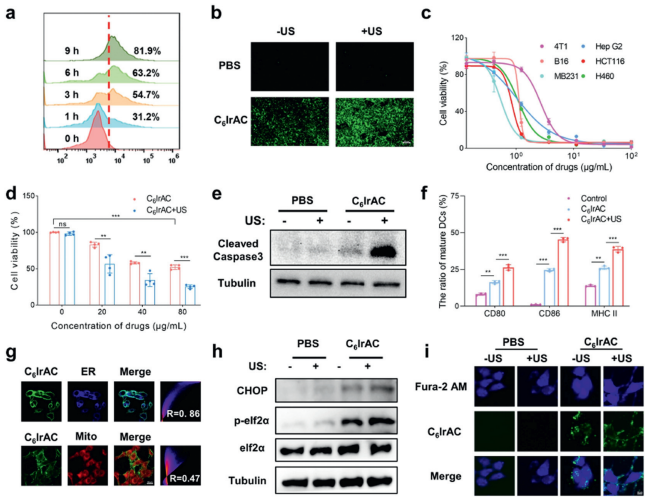


Fig. 2. Effects of C_6IrAC and DCs maturation *in vitro*. (a) Flow cytometry analysis of uptake behavior of C_6IrAC by 4T1 cells (C_6IrAC: 1 μg/mL). (b) Fluorescent images of intracellular ROS generation process in 4T1 cells after different treatments. Scale bar: 200 μm. (c) Determination of the IC_{50} values of C_6IrAC against six tumor cell lines ($n = 4$). (d) Viability of 4T1 cells after various treatments ($n = 4$). (e) WB analysis of cleaved caspase3 in 4T1 cells after different treatments. (f) Flow cytometric analysis of DCs maturation markers (CD80, CD86, MHC-II in DC 2.4) ($n = 3$). (g) Confocal co-localization images of C_6IrAC with ER and mitochondria. Green, C_6IrAC; Red, mitochondrial probe; Blue, ER probe. Scale bar: 50 μm. (h) WB analysis of typical ER stress-related proteins p-elf2α and CHOP in 4T1 cells after different treatments. (i) CLSM images of Ca^{2+} level in the cytoplasm of 4T1 cells after different treatments as detected by Fura-2 AM. Scale bar: 25 μm. ns, no significance. $^{*}P < 0.05$, $^{**}P < 0.01$, $^{***}P < 0.001$. Data are presented as mean ± standard deviation (SD).

robustly indicated that C_6IrAC produced ROS under US irradiation (Fig. 1d). Furthermore, the production of specific ROS species was confirmed using electron spin resonance (ESR) with 2,2,6,6-tetramethylpiperidine (TEMP) spin trap as a singlet oxygen ($^1O_2$) scavenger. The ESR spectra revealed a distinctive 1:1:1 peak ratio upon US exposure, which is indicative of the generation of $^1O_2$ by C_6IrAC (Fig. 1e and Figs. S2d and e in Supporting information). These findings substantiated the superior sonodynamic efficacy of C_6IrAC.

Accumulation of drugs within tumor cells is essential for cancer therapy. To evaluate the cellular uptake characteristics of C_6IrAC, C_6IrAC was incubated with 4T1 cells for various durations, and the changes in fluorescence intensity were assessed using flow cytometry and confocal laser scanning microscopy (CLSM) (Fig. S3 in Supporting information). As shown in Fig. 2a and Fig. S3a, the results indicate the concentration-dependent and time-dependent of C_6IrAC uptake by 4T1 cells. After 9 h co-incubation, the cellular uptake rate exceeded 80 %. CLSM imaging results corroborated these findings, suggesting that 4T1 cells exhibit a strong time-dependent cellular uptake of C_6IrAC (Fig. S3b).

Next, the DCFH-DA probe was utilized to stain 4T1 cells to investigate the production of ROS intracellularly. Flow cytometry results revealed that C_6IrAC induced ROS generation in 4T1 cells, which was further augmented following US exposure (Fig. S3c). Under fluorescence microscopy, cells co-incubated with C_6IrAC emerged green fluorescence, which was significantly enhanced post-US stimulation (Fig. 2b). It suggests that C_6IrAC possesses not only favorable sonodynamic properties but may also exhibit chemo-sensitivity to tumor cells. Consequently, we assessed the chemical toxicity of C_6IrAC against various tumor cell lines using a 72 h cell counting kit-8 (CCK8) assay (Fig. 2c). Notably, as shown in Table S2 (Supporting information), the IC_{50} values of C_6IrAC in multiple cancer cell lines were all <10 μg/mL. The cytotoxicity observed in tumor cells raises concerns regarding the biosafety profile of C_6IrAC. Gratifyingly, C_6IrAC demonstrated a higher safety profile in normal cells, such as 3T3 and HK2, compared to tumor cells (Fig. S3d). It may be attributed to the fact that the antioxidant defense systems in tumor cells are less effective than in normal cells, rendering them more vulnerable to increased ROS levels [33]. It suggests that C_6IrAC not only possesses favorable sonodynamic properties but also exhibits toxicity specifically towards tumor cells.

Subsequently, we investigated the SDT activity of C_6IrAC using the CCK8 assay *in vitro*. As depicted in Fig. 2d, C_6IrAC significantly inhibited cell viability upon co-culture for 24 h, with even more pronounced cytotoxicity observed under US stimulation. Coumarin 6 did not exhibit significant SDT activity at the same concentration and under the same ultrasonic conditions, demonstrating that C_6IrAC possesses superior sonosensitizing performance compared to coumarin 6 (Fig. S3e). Propidium iodide (PI) staining confirmed extensive cell death in 4T1 cells incubated with C_6IrAC following US exposure (Fig. S3f). To better understand the therapeutic mechanism of action of C_6IrAC, the protein levels of cleaved caspase-3 were investigated *via* Western blot (WB) analysis, indicating apoptosis in 4T1 cells following treatment with C_6IrAC, with US stimulation further enhancing the level of apoptosis (Fig. 2e). To more visually demonstrate the anti-tumor effects of C_6IrAC, 4T1 cells were stained with the Annexin V-fluorescein isothiocyanate (FITC)/propidium iodide (PI) kit post-treatment, and the apoptotic levels were assessed using flow cytometry, yielding results consistent with those from the WB (Fig. S3g). Additionally, wound-healing assays confirmed that C_6IrAC significantly inhibited tumor cell migration, with even greater inhibition observed under US stimulation (Figs. S4a and b in Supporting information). Thus, these findings demonstrated that C_6IrAC induces apoptosis in tumor cells and inhibits their metastasis, with the therapeutic efficacy of C_6IrAC being enhanced following US exposure.

DCs are considered a crucial link between innate and adaptive immunity. The differentiation and maturation of DCs can significantly augment anti-tumor immunity. Therefore, the *in vitro* effects of C_6IrAC on ICD were assessed by detecting the translocation of CRT and the secretion of HMGB1. In comparison to the control group cells where red fluorescence was nearly undetectable, there

was a significant upregulation of CRT expression in cells treated with C_6IrAC. Concurrently, we observed the release of HMGB1 from the nucleus relative to the control group, confirming the induction of ICD in 4T1 cells by C_6IrAC (Figs. S4c and d in Supporting information). Furthermore, a higher level of ICD was detected in the C_6IrAC+US group compared to the C_6IrAC group. Inspired by its potent ability to induce ICD, we co-cultured 4T1 cells with immature DC2.4 cells to verify whether ICD induced by C_6IrAC could promote the maturation of DCs. CD80, CD86 and MHC II are well-recognized markers of mature DCs [34]. We detected these surface markers using flow cytometry. As shown in Fig. 2f, the expression of CD80, CD86, and MHC II on DCs from the C_6IrAC and C_6IrAC+US groups was significantly upregulated compared to the control group, indicating maturation of the DCs. These results suggested that C_6IrAC can induce ICD in tumor cells and promote the maturation of DCs, while also acting as a SNS under US irradiation to further enhance DCs maturation. It provides evidence supporting the hypothesis that C_6IrAC promotes anti-tumor immunity.

The subcellular localization of the SNS within cells is a critical determinant in SDT, and we verified the subcellular localization of C_6IrAC by co-staining with the commercial dyes ER-Tracker Blue and Mito-Tracker Red. As shown in Fig. 2g, C_6IrAC specifically localized to ER ($R = 0.86$), as opposed to mitochondria ($R = 0.47$). The ER-localized C_6IrAC is anticipated to induce ER stress. Under US irradiation, the *in situ* generated ROS by C_6IrAC severely disrupt the ER, leading to a prominent oxidative stress. The phosphorylation of eukaryotic translation initiation factor 2α (elf2α) and the expression of C/EBP homology protein (CHOP) are markers of ER stress. WB analysis detected the changes of these two proteins in 4T1 cells following various treatments to further confirm this phenomenon. As expected, significant phosphorylation of elf2α and expression of CHOP were observed in both the C_6IrAC and C_6IrAC+US groups, indicating that C_6IrAC effectively initiated ER stress to eliminate tumor cells. The highest levels of elf2α phosphorylation and CHOP expression were noted in the C_6IrAC+US group, confirming that C_6IrAC-mediated SDT induced the further pronounced ER stress (Fig. 2h).

ER stress causes the massive release of Ca^{2+} from the ER, so intracellular Ca^{2+} levels were assessed by Ca^{2+} fluorescent probe (Fura-2 AM). Unlike other groups, the C_6IrAC and C_6IrAC+US groups exhibited significant blue fluorescence (Fig. 2i). The most intense fluorescence signal was observed in the C_6IrAC+US group, indicating the strongest ER stress induced by C_6IrAC post-US irradiation. The release of Ca^{2+} promotes the ER-mitochondria Ca^{2+} flux and leads to mitochondrial Ca^{2+} overload, inducing the opening of the mitochondrial permeability transition pore (mPTP), disrupting the electron transport chain, and ultimately generating a large amount of ROS, the scheme of mechanism was presented in Fig. S5a (Supporting information) [35]. Therefore, we examined the changes in mitochondrial membrane potential in 4T1 cells. The characteristic green-to-red (aggregates/monomers) images of JC-1 indicated a significant loss of membrane potential in the C_6IrAC and C_6IrAC+US groups (Fig. S5b in Supporting information). These findings elucidated that the underlying mechanism by which co-incubation with C_6IrAC leads to the generation of ROS within the cells.

To elucidate the underlining anti-tumor mechanisms of C_6IrAC, RNA-seq analysis was performed on 4T1 cells subjected to various treatments, encompassing a total of 24,355 genes (Fig. S6 in Supporting information). Fig. 3a depicts the results of a principal component analysis (PCA), where the data points from identical groups are observed to be closely clustered. This pattern of clustering is indicative of the robustness and consistency of the sequencing data. Differential expression analysis (DEA) was conducted between the PBS and C_6IrAC groups, revealing 3888 differentially expressed genes (DEGs), with 57.6% of these genes were downregulated in the C_6IrAC group (Fig. S6a). A similar analysis comparing the C_6IrAC and C_6IrAC+US groups identified 1343 DEGs, with 45.6% exhibiting downregulation in the C_6IrAC+US group (Fig. S6b). Heatmaps were utilized to provide a more intuitive representation of the gene expression differences (Figs. S6c and d). The Kyoto encyclopedia of genes and genomes (KEGG) was employed for a detailed analysis of the DEGs, with results presented in Fig. S7 (Supporting information). Subsequently, a comprehensive expression trend analysis (mfuzz) was conducted on the transcriptome data from the three groups (Fig. 3b). Based on gene ontology (GO), functional enrichment was performed to describe genes that were significantly downregulated in the C_6IrAC group and further downregulated in the C_6IrAC+US group (cluster 3), or those that were significantly upregulated in the C_6IrAC group and further upregulated in the C_6IrAC+US group (cluster 9).

Genes within cluster 3 were predominantly enriched in pathways related to hypoxia and mitochondrial function (Fig. 3c). Notably, in contrast to the traditional SDT-induced cellular hypoxia, C_6IrAC significantly inhibited the hypoxia pathway, with further inhibition observed post-US treatment. Gene set enrichment analysis (GSEA) corroborated the GO analysis results by assessing the expression of HIF-1 target genes and cellular hypoxia hallmarks (Figs. S8a and b in Supporting information). To validate these findings, we detect the protein levels of HIF-1α in 4T1 cells following different treatment modalities. The results indicated a significant reduction in HIF-1α levels in both the C_6IrAC and C_6IrAC+US groups compared to the PBS group, with the lowest levels observed in the C_6IrAC+US group (Fig. 3d). However, we did not detect catalase-like activity in C_6IrAC, suggesting that the decrease in HIF-1α protein levels was not attributable to the catalytic decomposition of H_2O_2 into O_2 by C_6IrAC (Fig. S8c in Supporting information). We hypothesize that heightened ER stress may lead to the proteasomal degradation of HIF-1α [18]. So, we used the proteasome inhibitor bortezomib (BTZ) to block the proteasomal pathway and reassessed HIF-1α levels. WB analysis confirmed that BTZ prevented HIF-1α degradation, indicating that C_6IrAC promotes the degradation of HIF-1α by activating its proteasomal pathway (Fig. 3e).

Genes in Cluster 9 were primarily enriched in pathways associated with oxidative stress and ER stress, which are integral to the anti-tumor mechanisms of C_6IrAC (Fig. 3f). Interestingly, these genes were found to be enriched in pathways involved in type I IFN production, a direct outcome of cGAS-STING pathway activation. Ifnb1 is a canonical downstream gene of the cGAS-STING pathway. Real time quantitative PCR (RT-qPCR) and enzyme linked immunosorbent assay (ELISA) indicated that C_6IrAC enhanced Ifnb1 mRNA and IFN-β protein levels (Fig. 3g and h). However, no significant difference was observed between the C_6IrAC and C_6IrAC+US groups. Expression of inflammatory cytokines controlled by the cGAS-STING pathway was also examined, showing a similar trend (Fig. 3i). WB analysis further confirmed a significant increase in the phosphorylation of STING and the expression of cGAS in both the C_6IrAC and C_6IrAC+US groups, substantiating the activation of the cGAS-STING pathway (Fig. 3j). We co-incubated C_6IrAC with 4T1 cells, and after with/without US treatment, the culture supernatant was added to the medium of RAW264.7 cells pre-treated with IL-4. CLSM imaging showed that C_6IrAC significantly enhanced the polarization of M2-type RAW264.7 cells to M1-type, and US treatment further promoted the level of M1 polarization. This indicates that C_6IrAC can promote the polarization of macrophages from M2 to M1, thereby activating innate antitumor immunity (Fig. S8d in Supporting information).

Cytoplasmic DNA is recognized by cGAS, and upon binding to DNA, cGAS activates the cGAS-STING pathway [36]. Inspired by the disruption of mitochondrial membrane potential by C_6IrAC, qPCR analysis was conducted to determine the cytoplasmic content of

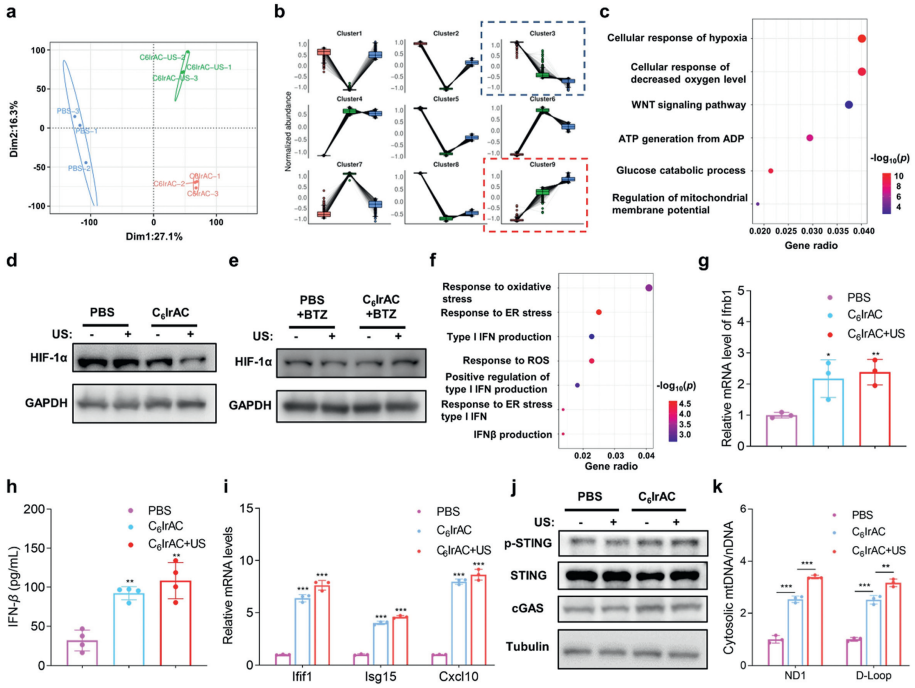


Fig. 3. C_6IrAC induces degradation of HIF-1α and activation of STING pathway. (a) PCA of the RNA-seq. PBS, C_6IrAC, and C_6IrAC+US groups were circled in blue, red, and green, respectively. (b) Mfuzz analysis of transcriptomic data from three distinct groups (PBS *vs.* C_6IrAC, $P < 0.05$ and fold change > 1.2). (c) GO analysis of genes in cluster 3. (d) WB analysis of HIF-1α in 4T1 cells after different treatments. (e) After BTZ treatment, western blot analysis of HIF-1α in 4T1 cells. GAPDH, glyceraldehyde-3-phosphate dehydrogenase. (f) GO analysis of genes in cluster 9. (g) RT-qPCR analysis depicting the relative expression levels of Ifnb1 in different groups ($n = 3$). (h) ELISA measurement of IFN-β concentration in the culture supernatant of 4T1 cells after different treatments ($n = 4$). (i) Representative RT-qPCR analysis depicting the relative expression levels of inflammatory cytokines in different groups ($n = 3$). (j) WB analysis of p-STING and cGAS in 4T1 cells after different treatments. (k) qPCR analysis of mtDNA release in the indicated 4T1 cells. The cytosol fraction was purified for qPCR analysis of mtDNA and nuclear DNA (nDNA). Two qPCR primers corresponding to the D-loop and ND-1 regions of mtDNA were used ($n = 3$). $^*P < 0.05$, $^{**}P < 0.01$, $^{***}P < 0.001$. Data are presented as mean ± SD.

mtDNA. The results demonstrated a significant increase in cytoplasmic mtDNA levels in both the C_6IrAC and C_6IrAC+US groups compared to the PBS group, with the highest levels observed in the C_6IrAC+US group (Fig. 3k). These findings suggested that ER stress induced by C_6IrAC disrupts mitochondrial membrane potential, leading to the translocation of mtDNA into the cytoplasm and subsequent activation of the cGAS-STING pathway. While the cytoplasmic mtDNA levels in the C_6IrAC+US group were significantly higher than in the C_6IrAC group, no corresponding increase in cGAS-STING pathway activation was observed. It could be due to the fact that the level of STING pathway activation is not entirely linearly correlated with the concentration of cytosolic mtDNA. Furthermore, an upregulation in the expression levels of genes associated with antigen presentation was detected, providing additional evidence for the hypothesis that C_6IrAC enhances anti-tumor immunity (Fig. S8e in Supporting information).

Therefore, we began to consider the possibility of C_6IrAC treatment for solid tumors *in vivo*. Considering the significant advantages of SDT in treating deep-seated tumors, we constructed the 3D tumor spheroids model to simulate solid tumors and investigated the penetration of C_6IrAC into solid tumor tissue (Fig. S9 in Supporting information). Images of the 3D tumor model were acquired using CLZM *Z*-stack, revealing that C_6IrAC exhibited good penetrative ability with a penetration depth exceeding 60 μm (Fig. S9a). Due to the excitation wavelength of C_6IrAC at 488 nm, which is unable to penetrate the interior of the tumor spheroid, imaging of deeper regions was not feasible. The AM/PI staining assay of the tumor spheroid confirmed the cytotoxicity of C_6IrAC towards deep tumor cells and demonstrated enhanced cytotoxicity under US stimulation (Fig. S9b).

To enhance the precision and efficiency of tumor therapy, we utilized fluorescence imaging to investigate the biodistribution of C_6IrAC and guide optimal treatment timing. All procedures involving the animals were conducted in compliance with the ethical standards and protocols established by the Xiamen University Animal Care and Use Committee (No. XMULAC20190146). C_6IrAC (5 mg/kg) was administered intravenously to 4T1 tumor-bearing mice. At 0, 4, 8, 12, 24, and 36 h post-injection, mice were euthanized at each time point for *ex vivo* fluorescence imaging of their major organs and tumor tissues (Fig. S9c). The results revealed a time-sensitive increase in the fluorescence intensity within the tumor area, reaching an optimal value at 24 h (Figs. S9d and e). At 36 h, a decrease in the fluorescence signal was observed in both major organs and tumor tissues, demonstrating the clearance of the drug from the body. In summary, C_6IrAC effectively penetrated and accumulated in the tumor and was metabolized and excreted after a certain period. It suggested that C_6IrAC holds exciting potential and biosafety for cancer therapy.

Next, we further evaluated potential of C_6IrAC for anti-tumor therapy *in vivo*. Seven-week-old BALB/c mice were randomly assigned to four experimental groups (PBS group, PBS+US group, C_6IrAC group and C_6IrAC+US group) to establish the 4T1 tumor-bearing model. The administered dose of C_6IrAC was 5 mg/kg, delivered *via* tail vein injection. *Ex vivo* fluorescence imaging results indicate that C_6IrAC exhibits the highest enrichment in the tumor region 24 h after tail vein injection. Therefore, the ultrasound wave (5 min, power density 1 W/cm^2, frequency 40 kHz) was performed 24 h after intravenous injection (Fig. 4a). Body weight and tumor size were monitored every 48 h. As depicted in Fig. 4b, tumor growth was significantly attenuated in the C_6IrAC and C_6IrAC+US groups compared to the PBS and PBS+US groups, with the most pronounced reduction observed in the C_6IrAC+US group. The weight of the tumors extracted on day 14 aligned with the volumetric growth patterns, demonstrating the favorable ther-

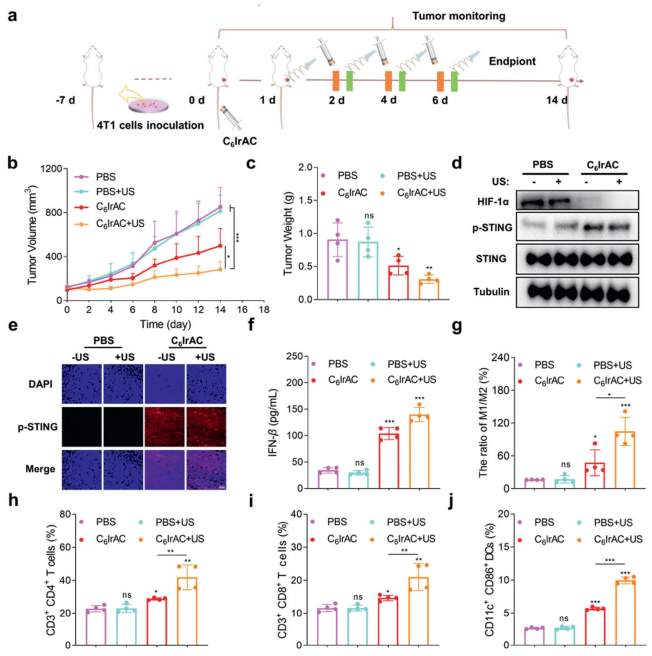


Fig. 4. Anti-tumor effects in 4T1 tumor-bearing mice *in vivo*. (a) Schematic of C_6IrAC-mediated therapy. (b) Tumor growth curves of 4T1 tumor-bearing mice after various treatments. (c) Tumor weights of each group on day 14 after treatment. (d) WB analysis of HIF-1α and p-STING levels in different tumor tissues. (e) p-STING staining results of tumor tissue sections of mice after different treatments. Scale bar: 100 μm. (f) Cytokine levels of IFN-β in the serum isolated from mice of each group at end of treatments. (g) The ratio of M1/M2 macrophages within 4T1 tumors. Flow cytometry analysis of $CD3^+CD4^+$, $CD3^+CD8^+$ T cells and $CD11c^+CD86^+$ cells in the lymph node (h–j) at day 14 after different treatments. Data are presented as mean ± SD ($n = 4$). $^*P < 0.05$, $^{**}P < 0.01$, $^{***}P < 0.001$.

apeutic outcome of C_6IrAC (Fig. 4c). Throughout the treatment period, there was no discernible impact on the body weight of mice treated with US and C_6IrAC, indicating no disruption to mice normal growth (Fig. S10a in Supporting information). After the treatment regimen, major organs from the mice, including the heart, liver, spleen, lungs and kidneys, were harvested and subjected to hematoxylin and eosin (H&E) staining to evaluate histological integrity. No overt organ damage was detected in the H&E-stained sections across all treatment groups (Fig. S10b in Supporting information). Hemolysis assays demonstrated that high concentrations of C_6IrAC did not induce erythrocyte lysis (Figs. S11a and b in Supporting information). Furthermore, a panel of blood markers, including alanine aminotransferase (ALT), creatine kinase MB (CK-MB), aspartate aminotransferase (AST) and creatinine (CREA), were comparable among the groups. These results substantiated that C_6IrAC, either alone or in conjunction with US, not only exerts robust anti-tumor efficacy but also maintains a favorable biosafety profile in murine models (Figs. S11c–f in Supporting information).

Inspired by the results of transcriptomic analysis, we conducted WB analysis on tumor tissues. The results revealed that HIF-1α was significantly downregulated in tumors from the C_6IrAC and C_6IrAC+US groups, with levels nearly undetectable in the C_6IrAC+US group (Fig. 4d). Concurrently, in alignment with *in vitro* experimental outcomes, the levels of p-STING were markedly elevated in the C_6IrAC and C_6IrAC+US groups compared to the PBS and PBS+US groups. IF staining of p-STING on tumor sections was performed. Consistent with the WB results, the STING pathway was significantly activated in the tumor cells of the C_6IrAC and C_6IrAC+US groups (Fig. 4e). Additionally, ELISA results indicated that IFN-β were significantly increased in the C_6IrAC and C_6IrAC+US groups compared to the other two groups (Fig. 4f). These results collectively demonstrate the activation of the cGAS-STING pathway in tumor cells *in vivo* by C_6IrAC. It has been reported that the activation of the cGAS-STING pathway can polarize M2-type macrophages ($F4/80^+$ $CD206^+$) towards M1-type macrophages ($F4/80^+$ $CD86^+$). Therefore, we analyzed the infiltrating macrophages in the tumor tissue by flow cytometry. The results indicated a higher M1/M2 ratio in the C_6IrAC and C_6IrAC+US groups, with the C_6IrAC+US group showing the highest ratio (Fig. 4g and Fig. S12 in Supporting information). These findings suggest that C_6IrAC promotes the polarization of infiltrating macrophages towards the M1 phenotype. However, the activation of the cGAS-STING pathway induced by C_6IrAC may not be the sole mechanism involved.

Subsequently, the main immune organs (lymph nodes and spleen) of the mice were collected and the *in vivo* immune activation potential of C_6IrAC was monitored by flow cytometry. The results demonstrated that a significant increase in the ratios of $CD3^+$ $CD8^+$ T cells, $CD3^+$ $CD4^+$ T cells and $CD11c^+$ $CD86^+$ DCs in the lymph nodes of the C_6IrAC and C_6IrAC+US groups, with the highest ratios observed in the C_6IrAC+US group (Figs. 4h–j and Fig. S13 in Supporting information). Concurrently, the trends in the spleen were consistent with those in the lymph nodes, indicating that C_6IrAC and its mediated SDT can enhance the anti-tumor immune response (Fig. S14 in Supporting information).

Beyond immune cells, cytokines such as tumor necrosis factor-alpha (TNF-α) and IFN-γ also play a significant role in tumor immunomodulation. Therefore, measuring the levels of TNF-α and IFN-γ secretion allows us to evaluate the immune response mediated by C_6IrAC (Fig. S15 in Supporting information). Serum levels of IFN-γ and TNF-α in mice from the C_6IrAC and C_6IrAC+US groups are significantly higher than those in the other two groups. The highest levels of cytokines were detected in the C_6IrAC+US group, suggesting that C_6IrAC could induce a robust cytokine-mediated immune response (Figs. S15a and b).

To further elucidate the anti-tumor mechanisms of C_6IrAC *in vivo*, we performed Ki67 and terminal deoxynucleotidyl transferase-mediated dUTP-biotin nick end labeling (TUNEL) staining on tumor sections. In Fig. S15c, the Ki67 staining results indicated the significant suppression of tumor proliferation in the C_6IrAC and C_6IrAC+US groups. Furthermore, the C_6IrAC+US group exhibited the most robust TUNEL fluorescence signal in tumor cells, indicating the most significant level of cell death. TUNEL signals were also detected in the C_6IrAC group, but no distinct signals were observed in the other two groups (Fig. S15d). Moreover, immunofluorescence analysis of tumor tissue sections was similarly employed to assess the immune response within the tumor microenvironment. CRT was found to be markedly expressed in the C_6IrAC and C_6IrAC+US groups, and the signal for HMGB1 was significantly diminished in these groups, indicating the enhanced ICD process (Fig. S15c). Compared to the PBS and PBS+US groups, the tumor tissues in the C_6IrAC and C_6IrAC+US groups displayed increased infiltration of $CD4^+$ T cells and $CD8^+$ T cells, with the highest infiltration observed in the C_6IrAC+US group (Fig. S15d). This observation suggests that a T-cell-mediated immune response was effectively triggered. These results suggested that C_6IrAC and its mediated SDT not only exhibit direct tumor-suppressive effects but also trigger a robust anti-tumor immune response through various pathways (ICD, activation of the STING pathway, *etc.*).

In this work, we synthesized a novel organometallic SNS (C_6IrAC), which specifically targets the ER. Besides, C_6IrAC exhibits tumor cell-specific cytotoxicity and excellent sonosensitivity. C_6IrAC induces ER stress in tumor cells, which is further amplified by US-mediated SDT through the *in situ* generation of a substantial amount of ROS. The strong oxidative stress induced significant apoptosis and prominent ICD. In-depth investigation into the underlying mechanisms of C_6IrAC revealed that it induces HIF-1α degradation, activates the cGAS-STING pathway, secretes IFN-

β, and upregulates the antigen presentation pathway. These multifaceted effects not only suppress the proliferation and migration of tumor cells but also enhance both innate and adaptive immunity. Furthermore, we evaluated the therapeutic efficacy of C_6IrAC in tumor models, demonstrating that it can induce activation of anti-tumor immune activation and reshape the tumor immune microenvironment. In summary, our research elucidates the excellent biomedical applications of C_6IrAC and showcases the prospects of ER-targeted SDT. Additionally, we deeply explored the therapeutic mechanisms of ER-targeted SDT through transcriptomics, clarifying the biological properties of this organometallic SNS molecule. Therefore, we believe that our current research provides an innovative strategy for the design and development of SNS, with significant clinical translational potential.

Declaration of competing interest

The authors declare that they have no known competing financial interests or personal relationships that could have appeared to influence the work reported in this paper.

CRediT authorship contribution statement

Yubo Tan: Writing – original draft, Project administration, Methodology, Investigation, Conceptualization. **Ziying Wang:** Software, Resources, Project administration, Formal analysis. **Yibo An:** Resources, Project administration, Investigation. **Man Li:** Methodology, Investigation, Formal analysis. **Dazhuang Xu:** Validation, Supervision, Software. **Renyuan Liu:** Methodology, Investigation, Data curation. **Xinyu Tan:** Software, Resources, Investigation. **Yaohui He:** Writing – original draft, Software, Funding acquisition, Data curation. **Zhixiang Lu:** Writing – review & editing, Project administration, Funding acquisition. **Gang Liu:** Writing – review & editing, Project administration, Funding acquisition, Conceptualization.

Acknowledgments

This work was supported by the National Key Research and Development Program of China (Nos. 2023YFB3810000, 2023YFC241570), the National Natural Science Foundation of China (NSFC, Nos. 32101113, 81925019, 82203476, U22A20333), the Natural Science Foundation of Sichuan Province (No. 2024NSFSC1741) and the China Postdoctoral Science Foundation (No. 2022M712661).

Supplementary materials

Supplementary material associated with this article can be found, in the online version, at doi:10.1016/j.cclet.2025.111214.

References

[1] H. Shibaguchi, H. Tsuru, M. Kuroki, M. Kuroki, Anticancer Res. 31 (2011) 2425–2429.
[2] I. Rosenthal, J.Z. Sostaric, P. Riesz, Ultrason. Sonochem. 11 (2004) 349–363.
[3] S. Liang, X. Deng, P. Ma, Z. Cheng, J. Lin, Adv. Mater. 32 (2020) e2003214.
[4] Z. Gao, J. Zheng, B. Yang, et al., Cancer Lett. 335 (2013) 93–99.
[5] S. Wang, Z. Hu, X. Wang, et al., Ultrasound Med. Biol. 40 (2014) 2125–2133.
[6] Q. Zhang, C. Bao, X. Cai, et al., Cancer Sci. 109 (2018) 1330–1345.
[7] W. Um, H. Ko, D.G. You, et al., Adv. Mater. 32 (2020) e1907953.
[8] Y. Yang, J. Huang, M. Liu, et al., Adv. Sci. 10 (2023) e2204365.
[9] S. Liu, J. Ma, A. Wang, N. Zheng, Chin. Chem. Lett. 36 (2025) 110032.
[10] G. Kroemer, C. Galassi, L. Zitvogel, L. Galluzzi, Nat. Immunol. 23 (2022) 487–500.
[11] Q. Zhao, Y. Zhao, S. Zhong, et al., Chin. Chem. Lett. 35 (2024) 109644.
[12] J. Fucikova, O. Kepp, L. Kasikova, et al., Cell Death Dis. 11 (2020) 1013.
[13] W. Xiong, P. Wang, J. Hu, et al., Sci. Rep. 5 (2015) 17485.
[14] F. Gong, L. Cheng, N. Yang, et al., Nat. Commun. 11 (2020) 3712.
[15] Z. Luo, M. Tian, G. Yang, et al., Signal Transduct. Target. Ther. 7 (2022) 218.
[16] S.J. Cowman, M.Y. Koh, Trends Cancer 8 (2022) 28–42.
[17] B. Zhang, L. Lin, J. Mao, et al., Chin. Chem. Lett. 34 (2023) 108518.
[18] D. Mennerich, K. Kubaichuk, G.S. Raza, et al., Redox Biol. 50 (2022) 102243.
[19] H. Deng, Z. Zhou, W. Yang, et al., Nano Lett. 20 (2020) 1928–1933.
[20] J.A. Smith, Front. Immunol. 11 (2020) 611347.
[21] L. Sun, J. Wu, F. Du, X. Chen, Z.J. Chen, Science 339 (2013) 786–791.
[22] L. Ou, A. Zhang, Y. Cheng, Y. Chen, Front. Immunol. 12 (2021) 795048.
[23] J. Wang, S. Li, M. Wang, et al., Sci. Immunol. 9 (2024) eadj3945.
[24] R. Falahat, A. Berglund, P. Perez-Villarroel, et al., Nat. Commun. 14 (2023) 1573.
[25] J. Hu, F.J. Sanchez-Rivera, Z. Wang, et al., Nature 616 (2023) 806–813.
[26] C. Li, Y. Zhang, Y. Wan, et al., Chin. Chem. Lett. 32 (2021) 1615–1625.
[27] Q. Wang, J.S. Bergholz, L. Ding, et al., Nat. Commun. 13 (2022) 3022.
[28] A.A. Mandal, R. Kushwaha, A.K. Yadav, S. Banerjee, ChemBioChem 14 (2023) e202200597.
[29] J. Jiang, X. Cui, Y. Huang, et al., Nano Biomed. Eng. 16 (2024) 152–187.
[30] X. Wang, X. Zhong, L. Bai, et al., J. Am. Chem. Soc. 142 (2020) 6527–6537.
[31] P. Ho, C. Ho, W. Wong, Coord. Chem. Rev. 413 (2020) 213267.
[32] H. Cui, W. Zhu, C. Yue, et al., Chin. Chem. Lett. 35 (2024) 109727.
[33] E.C. Cheung, K.H. Vousden, Nat. Rev. Cancer 22 (2022) 280–297.
[34] S. Bai, Z. Lu, Y. Jiang, et al., ACS Nano 16 (2022) 997–1012.
[35] M. Kerkhofs, M. Bittremieux, G. Morciano, et al., Cell Death Dis. 9 (2018) 334.
[36] A. Decout, J.D. Katz, S. Venkatraman, A. Ablasser, Nat. Rev. Immunol. 21 (2021) 548–569.